Journal of Biomedical Optics

BiomedicalOptics.SPIEDigitalLibrary.org

Quantum dot imaging in the second near-infrared optical window: studies on reflectance fluorescence imaging depths by effective fluence rate and multiple image acquisition

Yebin Jung
Sanghwa Jeong
Won Nayoun
Boeun Ahn
Jungheon Kwag
Sang Geol Kim
Sungjee Kim

SPIE.

Quantum dot imaging in the second near-infrared optical window: studies on reflectance fluorescence imaging depths by effective fluence rate and multiple image acquisition

Yebin Jung,[a] Sanghwa Jeong,[a] Won Nayoun,[a,†] Boeun Ahn,[a] Jungheon Kwag,[b] Sang Geol Kim,[c] and Sungjee Kim[a,b,*]

[a]Pohang University of Science and Technology, Department of Chemistry, 77 Cheongam-ro, Nam-gu, Pohang 790-784, Republic of Korea
[b]Pohang University of Science and Technology, School of Interdisciplinary Bioscience and Bioengineering, 77 Cheongam-ro, Nam-gu, Pohang 790-784, Republic of Korea
[c]Kyungpook National University, School of Medicine, Department of Surgery, 680 Gukchaebosang-ro, Joong-gu, Daegu 700-422, Republic of Korea

Abstract. Quantum dot (QD) imaging capability was investigated by the imaging depth at a near-infrared second optical window (SOW; 1000 to 1400 nm) using time-modulated pulsed laser excitations to control the effective fluence rate. Various media, such as liquid phantoms, tissues, and *in vivo* small animals, were used and the imaging depths were compared with our predicted values. The QD imaging depth under excitation of continuous 20 mW/cm^2 laser was determined to be 10.3 mm for 2 wt% hemoglobin phantom medium and 5.85 mm for 1 wt% intralipid phantom, which were extended by more than two times on increasing the effective fluence rate to 2000 mW/cm^2. Bovine liver and porcine skin tissues also showed similar enhancement in the contrast-to-noise ratio (CNR) values. A QD sample was inserted into the abdomen of a mouse. With a higher effective fluence rate, the CNR increased more than twofold and the QD sample became clearly visualized, which was completely undetectable under continuous excitation. Multiple acquisitions of QD images and averaging process pixel by pixel were performed to overcome the thermal noise issue of the detector in SOW, which yielded significant enhancement in the imaging capability, showing up to a 1.5 times increase in the CNR. [DOI: 10.1117/1.JBO.20.4.046012]

Keywords: quantum dots; infrared imaging; charge-coupled devices; fluorescence; image enhancement.

Paper 150042R received Jan. 26, 2015; accepted for publication Apr. 2, 2015; published online Apr. 28, 2015.

1 Introduction

Near-infrared (NIR) *in vivo* imaging with semiconductor quantum dots (QDs) can offer nonradioactive extraction of biological information, which can be applicable to real-time multiplexed imaging for studies of biological phenomena and potentially in the field of medicine, such as for surgery. Conventional reflectance fluorescence imaging typically shows the tissue penetration depth in the order of a few to tens of milimeters.[1,2] The degrees of absorption, scattering, and autofluorescence vary dramatically depending on the wavelength of light. The NIR optical window, the wavelength region from 700 to 1400 nm, can maximize the tissue penetration depths because of the minimal interference by the absorption and scattering from water and biological tissues.[3,4] The NIR optical window can be divided into the first optical window (FOW; 700 to 900 nm) and the second optical window (SOW; 1000 to 1400 nm). The SOW can especially be more advantageous for deep tissue penetrations than the FOW because of the reduced scattering.[5–7] In 2003, simple simulation studies of optical imaging in turbid media, such as tissue or blood, showed that it would be possible to improve the signal-to-noise ratios by over 100-fold by fluorophores that emit at SOW when compared with those that emit at FOW. Penetration depth, which is defined as the depth at which the light intensity is attenuated to $1/e$ times the original intensity, has little meaning for practical imaging applications. As discussed in our previous study, imaging depth can be defined by the ability to distinguish an object from the background.[6] QDs having emission spectra in FOW or SOW were placed under biological tissues for comparison of the imaging depths. QD imaging in SOW showed significantly extended imaging depths over the QD imaging in FOW. In highly scattering media, such as skin tissue, the SOW QD imaging depth was larger than that of FOW more than threefold, mostly because of the reduced scattering in SOW. In highly absorbing media, such as the liver, the SOW QD imaging depth could be extended by 1.4 times over that of FOW QD imaging by switching the excitation to a longer wavelength.

QDs are practically the only class among imaging contrast agents that can be bright and wavelength-tunable in the NIR SOW. Organic dyes[8] and fluorescent proteins intrinsically suffer from the molecular vibration-coupled nonradiative channels,

*Address all correspondence to: Sungjee Kim, E-mail: sungjee@postech.ac.kr

†Current address: Samsung Advanced Institute of Technology, 130 Samsung-ro, Yeongtong-gu, Suwon-si 443-803, Republic of Korea.

which makes them nonfluorescent at NIR SOW. Lanthanide complexes[9] and single-walled carbon nanotubes[10] show weak emissions in NIR SOW, and it is very difficult to tailor the emission wavelength. QDs can reach a photoluminescence quantum yield (QY) as high as 90% in NIR SOW.[11] Recent advances in the QD synthesis replaced many heavy metal elements in QDs with potentially safer elements.[12–16] Recently, Ag_2S QDs have been reported and are attracting much interest for NIR SOW imaging.[17,18]

QD imaging depth is affected by a large number of parameters, including factors from the incident light, such as incident angle, polarization, and fluence rate, and those from QDs, such as the concentration, QY, and absorption cross-section. The fluence rate of incident light is a critical parameter that can be tuned to enhance the imaging depth at the cost of relatively little effort. In principle, the photon penetration depth should be independent of the power of the incident light.[19] However, in reality and especially when using an InGaAs charge-coupled device (CCD) for SOW, imaging depth is dependent on the fluence rate because of thermal noise: as tissue thickness increases, the exposure time required for optimal imaging increases, thus, the thermal noise effect increases. As a result, a higher incident light intensity can increase the imaging depth. Our previous study showed the imaging depth increase by 1.4 times in liver and by 1.8 times in skin tissue by increasing the fluence rate of the incident light from 3 to 20 mW/cm^2.[6] Because excessive intensity of the incident light can cause side effects, such as shrinkage of collagen, reduction of enzymatic activity, and burning,[20] human access during operation is regulated. According to the U.S. Food and Drug Administration (FDA), continuous human access is permitted up to 0.5 W at the visible and NIR wavelengths.[6,21] Noncontinuous pulsed excitations that are synchronized with the detector can raise the effective fluence rate and, thus, extend the imaging depth while circumventing the side effects. We have built an NIR SOW imaging system equipped with time-modulated pulsed laser excitations synchronized with an InGaAs CCD to investigate the imaging depths attainable by increasing the effective fluence rate. A PbS QD emitting at 1300 nm was synthesized and used as a model contrast agent at NIR SOW. The QD imaging depth was obtained in various media such as liquid phantoms, tissues, and small animal *in vivo* experiment setups. The imaging depth values were also compared and discussed with the expected values previously obtained by simulations. In addition, multiple acquisitions of QD fluorescence images were performed to enhance the imaging capabilities by image averaging. QD fluorescence images under an identical experimental condition were repeatedly captured, and an averaged image was obtained by overlapping and averaging the fluorescence intensities pixel by pixel. The image averaging yielded significant enhancement in the imaging capability showing up to a 1.5 times increase in the contrast-to-noise ratio (CNR); however, the enhancement applied only for cases of the intermediate contrast-to-noise level.

2 Materials and Methods

2.1 *Materials*

Lead(II) acetate trihydrate, oleic acid, 1-octadecene, bis(trimethylsilyl)sulfide, hemoglobin from bovine blood, and intralipid (20% emulsion) were purchased from Sigma-Aldrich.

2.2 *Synthesis of PbS Quantum Dots*

PbS QDs were prepared by following a previously reported method.[22] The sulfur precursor was prepared by mixing bis(trimethylsilyl)sulfide (0.1 mmol) with 1-octadecene (5 mL) in the glove box. Lead(II) acetate trihydrate (1 mmol), oleic acid (10 mmol), and 6.8 mL of 1-octadecene were loaded to a three-neck flask and activated at 180°C for 1 h. The lead precursor solution was cooled down to 100°C and the temperature was maintained for 1 h under vacuum for degassing. The solution was heated to 150°C, and the sulfur precursor solution was quickly injected into the reaction flask. The temperature was maintained at 120°C, and the solution was stirred until the desired size of the PbS QD was obtained. The reaction solution was cooled down to room temperature and diluted with chloroform. The synthesized PbS QDs showed an emission peak at 1300 nm and the QY was 27%.

2.3 *Image Data Process*

The thresholding process was conducted using the MATLAB® (The MatWorks, Inc.) program based on the global thresholding algorithm.[23] The raw intensity data of NIR fluorescence images were imported to MATLAB®. The histogram of the image was divided into two regions. One is the group of pixels with a higher or the same intensity of the threshold value, and the other is that of pixels with a lower intensity. The histogram of the image was divided into the two regions using the threshold value, and the mean intensities of the two regions were obtained. A new threshold was created with the means of the two regions. These processes were iterated until the threshold value converged. The pixels that have the same or higher intensity than the threshold were regarded as the signal and the other pixels were regarded as the background.

An image averaging process was conducted using the MATLAB® program. NIR fluorescence images for the averaging were obtained by multiple acquisitions using identical experimental conditions. The time lapse between acquisitions was <2 s. The raw intensity data of images were imported to MATLAB®. The averaged image was constructed by pixel-by-pixel averaging the intensity values of each pixel position using all images of the multiple acquisitions.

2.4 *Imaging Setup*

A glass container with 1 cm lateral dimension was filled with PbS QD chloroform solution and was submerged in the liquid phantom solution or biological tissues at a depth z below the air/solution or air/tissue interface. Bovine liver tissues and porcine skin tissues were obtained from the local butchers, and the thicknesses were measured by Vernier calipers. The light source emitting 915 nm laser (Changchun New Industries, FC-W-915) has an incidence angle of 30 deg with respect to the detector that is perpendicular to the air/tissue interface. Light intensity was measured with a digital optical power meter (Thorlabs, PM100). An InGaAs CCD camera (FLIR, SC2500-NIR) was used for the SOW imaging. A 1000 nm long-pass filter (Thorlabs, FEL1000) and a zoom lens (Navitar, 1-60135-IR) were attached in front of the CCD camera. The working distance between the samples and the zoom lens was ~40 cm and the field of view was 5×5 cm^2. The light source and InGaAs CCD camera were synchronized with a trigger signal using a data acquisition board (National Instruments, NI USB-6353).

2.5 *In Vivo Imaging Experiment*

A female nude mouse (BALB-c-nu/nu, 22 g, Orientbio Co. Ltd., Korea) was used in accordance with our institution's guidelines on animal care and use. The mouse was anesthetized with 0.02 mL g^{-1} of intraperitoneal tribromoethanol (Avertin). A glass cylinder with a 5 mm lateral dimension was filled with 0.3 mL PbS QD solution in chloroform and capped with a rubber septa. The cylinder was inserted into the abdominal cavity of the mouse parallel to the spinal column. The incision was sutured with stitching fiber. The InGaAs CCD camera was used for the NIR fluorescent imaging, and the visible CCD (Hitachi Kokusai Electric Inc., HV- D37A) was used for the color imaging.

3 Results and Discussion

3.1 *QD Imaging Depth at NIR SOW by Effective Fluence Rate: Experimental Setup and Liquid Phantom Studies*

NIR photons are known to penetrate ~10 cm in biological tissues.[4] However, the optical imaging depth is often much smaller than the photon penetration depth mostly because of the blur and distortion caused by scattering. To quantify the imaging capabilities, the signal intensity over the background noise fluctuation and the spatial resolving power should be considered.[6] The criterion is often assessed by the CNR, which is defined as the difference between the signal intensity and the background intensity divided by the standard deviation of the background intensity. The Rose criterion states that, to be detectable, the CNR of an object should exceed 4.[24,25] In order to determine the CNR, we have adopted a simple image data process of segmentation by global thresholding. We have built a QD imaging system for NIR SOW equipped with a time-modulated laser synchronized with the CCD. It is a reflectance fluorescence imaging system with a planar geometry, controlled by a trigger signal for the synchronization between the laser pulse and CCD capture [Fig. 1(a)]. Reflectance fluorescence imaging (rather than a back-illuminating configuration) was used to obtain information that is more relevant for potential intraoperative applications. The laser illuminates the imaging surface at a 30 deg incidence angle, which provides the best imaging capability because of the minimal scattering and reflection at the air/tissue interface.[6] We have adopted a single-photon fluorescence imaging modality for simplicity; however, our system should also be applicable to two-photon or multiphoton imaging. QDs have large multiphoton absorption cross-sections, and multiphoton QD imaging is expected to provide deeper imaging depths with less overall photobleaching. Webb and coworkers have demonstrated dynamic visualization through the skin of living mice in capillaries hundreds of micrometers deep.[26] Medintz and coworkers showcased QD-coated glass pipettes that provided strong two-photon contrast at deeper penetration depths than those achievable with current methods and have demonstrated single-cell electroporation of identified rat and mouse neurons *in vivo*.[27]

Fluorescence imaging from the field was collected by the zoom lens and was divided by a dichroic mirror: the visible part went to a color CCD and the NIR part to an InGaAs CCD. The InGaAs CCD was synchronized with the laser and was programmed to capture the fluorescence image only during the laser excitations. 1300 nm emitting PbS QD was used for the NIR SOW emission. PbS QD was chosen because its synthetic route is relatively well known. Our values for the imaging depth

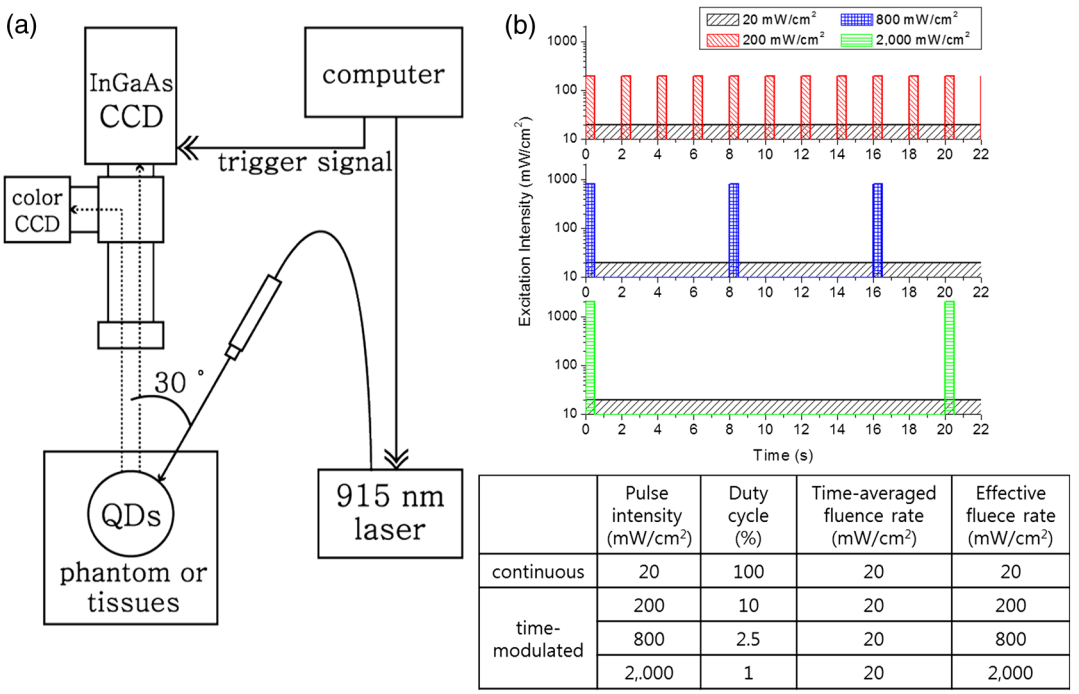

	Pulse intensity (mW/cm^2)	Duty cycle (%)	Time-averaged fluence rate (mW/cm^2)	Effective fluece rate (mW/cm^2)
continuous	20	100	20	20
time-modulated	200	10	20	200
	800	2.5	20	800
	2,.000	1	20	2,000

Fig. 1 (a) Schematic diagram of the experimental setup for near-infrared fluorescence imaging of quantum dot samples in liquid phantom or tissue. (b) A graph showing the excitation intensity profile over time under continuous and under different pulsed excitations of time-modulated square waves. The table below lists the pulse intensity, duty cycle, time-averaged fluence rate, and effective fluence rate for each excitation case.

are not confined to the QD material choice and can be easily extended to other NIR SOW QDs, such as Ag_2S QDs. Because QDs will likely be used in the future for tumor targeting based diagnosis, and specifically for detection of small collections of malignant cells, we have simulated them using a glass container of 1 cm lateral dimension filled with the PbS QD chloroform solution. The cylindrical glass container is designed to simulate a 1 cm spherical solid tumor, which is often a critical detection criterion in cancer diagnosis. The concentration of PbS QD solution was 1 μM, and QY was measured to be 27% using a secondary method comparing the integrated emission intensity of QDs to that of organic dye IR-26 (QY = 0.5%) at the same excitation wavelength and optical density.[28] Hemoglobin and intralipid liquid phantoms were used to simulate tissues that are dominantly absorbing and scattering, respectively. The liquid phantom was prepared by dispersing hemoglobin powder or intralipid solution in deionized water, and the attenuation coefficient of the phantom was measured in the visible and NIR regions. The attenuation coefficient values were compared with the values of tissues.[29] 2 wt% hemoglobin and 1 wt% intralipid phantoms were used for our study because they can represent liver and skin tissues, respectively.

A 915 nm solid-state laser was used for time-modulated excitations. The FDA allows a radiant power of 0.5 W for continuous irradiation in the 400 to 1400 nm range. For pulsed light, 40 W/cm^2 radiant exposure is allowed with a maximal 0.25 s pulse length.[21] In our 5 × 5 cm^2 field of view, the maximal FDA allowed a radiant power corresponding to a continuous 20 mW/cm^2. The fluence rate of 20 mW/cm^2 was used for our standard fluence rate. For time-modulated illuminations, repeated square-wave laser pulses with a duration of 200 ms were generated with pulse intensities of 200, 800, or 2000 mW/cm^2. The pulse repetition rate (or duty cycle) was adjusted so that the time-averaged fluence rate for all the cases will be a constant 20 mW/cm^2 [Fig. 1(b)]. The duty cycle is defined by the ratio between the pulse duration time over the excitation period. The continuous wave and time-modulated waves are the same for the time-averaged fluence rate, which is presented by the cumulative area of bars for enough time duration for each excitation condition in Fig. 1(b).

The QD cylinder was immersed in the liquid phantom to a depth (i.e, liquid phantom thickness) varying from 0 to 25 mm. The excitation condition was 20/100, 200/10, 800/2.5, or 2000/1 by the laser on-state fluence rate (mW/cm^2) / the duty cycle (%) [Fig. 1(b)]. Though the time-averaged fluence rates are the same for all the excitation conditions, the effective fluence rate should simply follow the laser pulse intensity. Reflectance fluorescence images were taken for the QD sample in the hemoglobin or

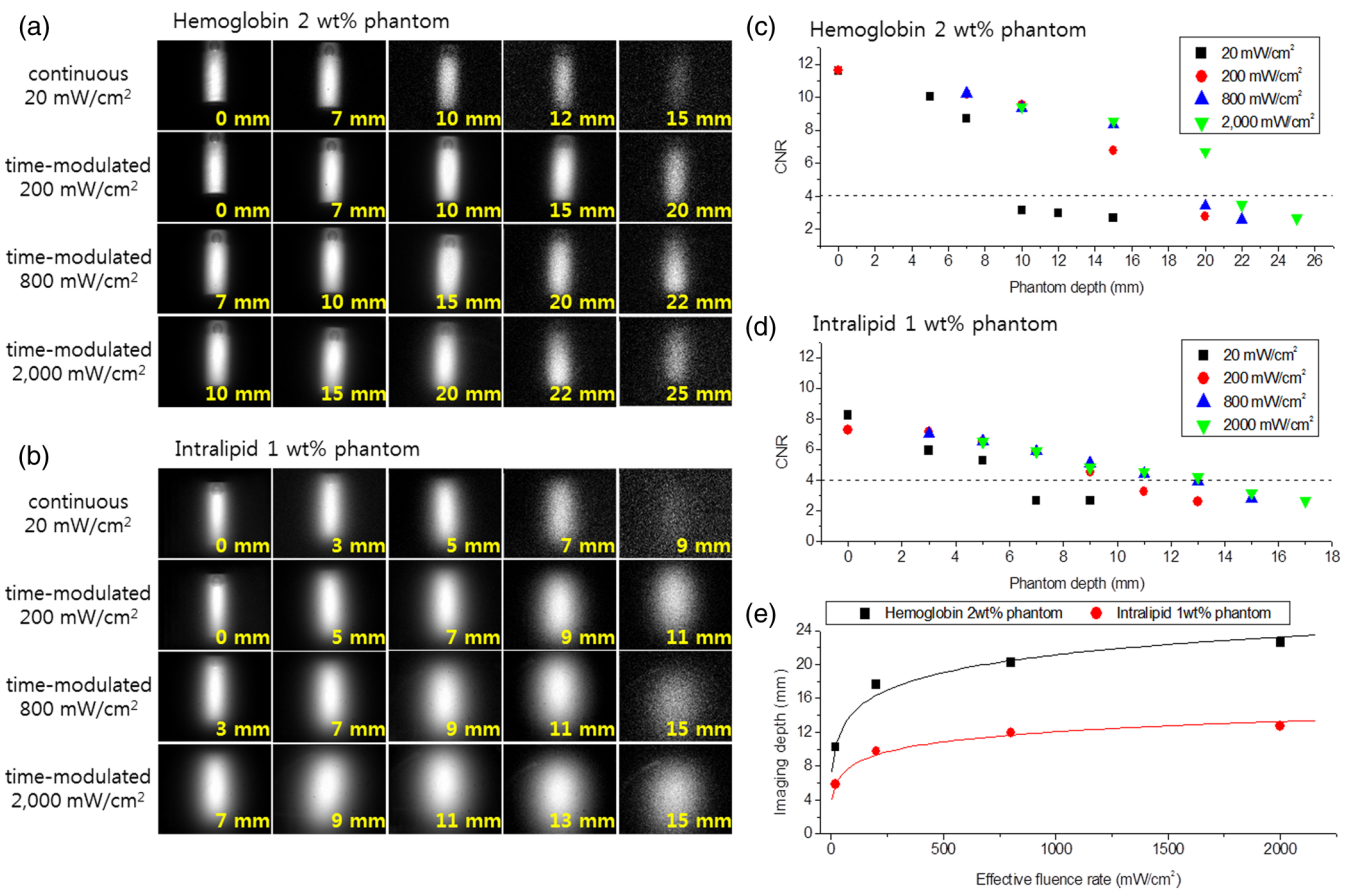

Fig. 2 Imaging capabilities under different excitations of continuous 20 mW/cm^2, time-modulated pulsed 200, 800, and 2000 mW/cm^2 in liquid phantom. Near-infrared fluorescence images (a) for 2 wt% hemoglobin phantom experiments and (b) for intralipid 1 wt% phantom experiments. The phantom thickness covering the quantum dot (QD) solution is presented on the bottom right of each fluorescence image. Contrast-to-noise ratios (CNRs) for different phantom depths of (c) the hemoglobin phantom and (d) the intralipid phantom. Dotted lines in the graph represent imaging depth criteria. (e) Imaging depths obtained by the hemoglobin and intralipid phantom studies.

intralipid phantom as the phantom thickness increased [Figs. 2(a) and 2(b)]. For both phantoms, the QD signal was reduced and the image became blurred as the phantom thickness increased. In Figs. 2(a) and 2(b), it is noted that each column is not aligned for the same phantom thickness. The thickness is noted in the right bottom of each panel. As the effective fluence rate increased, the fluorescence image showed more contrast. For an example, the QD cylinder under 15 mm hemoglobin phantom that was hardly detectable under the continuous 20 mW/cm^2 condition, became quite visible under pulse 200 mW/cm^2 condition and was very clear and crisp under pulse 800 or 2000 mW/cm^2 conditions. For the 15 mm thickness hemoglobin phantom case, the CNR values were 2.69 for the continuous 20 mW/cm^2 excitation and became 6.75, 8.34, and 8.56 for the pulsed 200, 800, and 2000 mW/cm^2 conditions, respectively. The CNR values versus hemoglobin phantom thickness were plotted for the different excitation conditions [Fig. 2(c)]. Using the Rose criterion and the intrapolation that we had previously reported, the imaging depths were obtained for different excitation conditions. The imaging depth was 10.3 mm for the continuous 20 mW/cm^2 excitation. The imaging depth was extended to 17.6, 20.2, and 22.6 mm as pulsed excitations of the intensity 200, 800, and 2000 mW/cm^2 were applied [Fig. 2(e)]. We have previously obtained the NIR SOW QD imaging depths by different excitation fluence rates at a low power regime and have used the results to predict the values for higher fluence rates (Table 1).[6] Our results in the 2 wt% hemoglobin phantom showed 1.71 and 2.19 times increases in the imaging depth upon increasing the effective fluence rate from 20 to 200 and 2000 mW/cm^2, respectively. For such an effective fluence rate increase from 20 to 200 and 2000 mW/cm^2 in bovine liver tissues, we previously predicted 1.22 and 1.44 times imaging depth enhancement. The larger relative imaging depth enhancement observed for our hemoglobin liquid phantom over the previous prediction for bovine liver tissue is thought to be attributed to different experimental conditions. Previously predicted values were obtained from conditions quite different from those adopted for the experiment herein, such as the QD concentration and QY. The relative imaging depth change by the effective fluence rate increase is considered to not be significantly altered by the QD concentration and QY. However, the excitation wavelength may play a critical role. By previously upgrading the excitation source from light-emitting diodes to a pulse laser for time-modulation, we have switched the excitation wavelength from 850 to 915 nm. The longer excitation wavelength may have resulted in the larger relative imaging depth enhancement at higher effective fluence rate excitations. The dissimilarity between the liquid phantom and liver tissue might also have contributed.

The QD cylinder in the intralipid phantom was imaged highly blurred as the thickness increased [Fig. 2(b)]. As the effective fluence rate increased, the fluorescence image showed more contrast between the signal image and the background. For example, the QD cylinder under 7 and 9 mm the intralipid phantom was hardly detectable under the continuous 20 mW/cm^2 excitation, but became more visible as the effective fluence rate increased to 200, 800, and 2000 mW/cm^2. For the 7 mm thickness intralipid phantom case, the CNR values were 2.67 for the continuous 20 mW/cm^2 and became 5.84, 5.87, and 5.89 for the pulsed 200, 800, and 2000 mW/cm^2 conditions, respectively. The CNR values versus intralipid phantom thickness was plotted [Fig. 2(d)], and the imaging depths were obtained. The imaging depth was 5.84 mm for the continuous 20 mW/cm^2 excitation, which was extended to 9.24, 12.7, and 16.0 mm as pulsed excitations of the intensity 200, 800, and 2000 mW/cm^2 were applied [Fig. 2(e)]. Our results with the 1 wt% intralipid phantom showed 1.66 and 2.19 times increases in the imaging depth when increasing the effective fluence rate from 20 to 200 and 2000 mW/cm^2, respectively. In porcine skin tissues, our previous predictions were 1.43 and 1.87 times increases for such cases. The larger relative imaging depth enhancement over our previous predictions can be attributed to the same reasons as discussed for the hemoglobin phantom experiment. The hemoglobin phantom showed deeper imaging depths than the intralipid phantom because the hemoglobin phantom has a lower attenuation coefficient than the intralipid phantom.

3.2 *NIR SOW QD Imaging: Tissue Phantom Studies and In Vivo Animal Cases*

The QD cylinder was placed under real tissues to validate the liquid phantoms. 13-mm-thick bovine liver tissue and 14 mm porcine skin tissues were placed on top of the QD cylinder and the image was taken under the excitations of a continuous 20 mW/cm^2 or pulsed excitations of 200 or 2000 mW/cm^2 [Fig. 3(a)]. For the continuous 20 mW/cm^2 excitation, an almost undetectable and dim fluorescence image was observed and the CNR was 2.64 for the liver and 2.65 for the skin. The CNR values were below the Rose criterion and the signal images

Table 1 Measured imaging depths in liquid phantoms and predicted imaging depths from the reference in biological tissues under different experimental conditions.

	Imaging depth (mm) under the effective fluence rate (mW/cm^2) of: (Ratio to the value of 20 mW/cm^2 case)			
Medium	20	200	2000	Remarks
Hemoglobin 2 wt% phantom	10.3 (1.00)	17.6 (1.71)	22.6 (2.19)	Experimental data QD QY 27%
Intralipid 1 wt% phantom	5.85 (1.00)	9.74 (1.66)	12.8 (2.19)	Concentration 1.0 μM, 915 nm excitation
Bovine liver tissue	29.7 (1.00)	36.3 (1.22)	42.9 (1.44)	Predicted values from Ref. 6 QD QY 50%,
Porcine skin tissue	17.5 (1.00)	25.1 (1.43)	32.8 (1.87)	Concentration 10.0 μM, 850 nm excitation

Note: QD, quantum dot; QY, quantum yield.

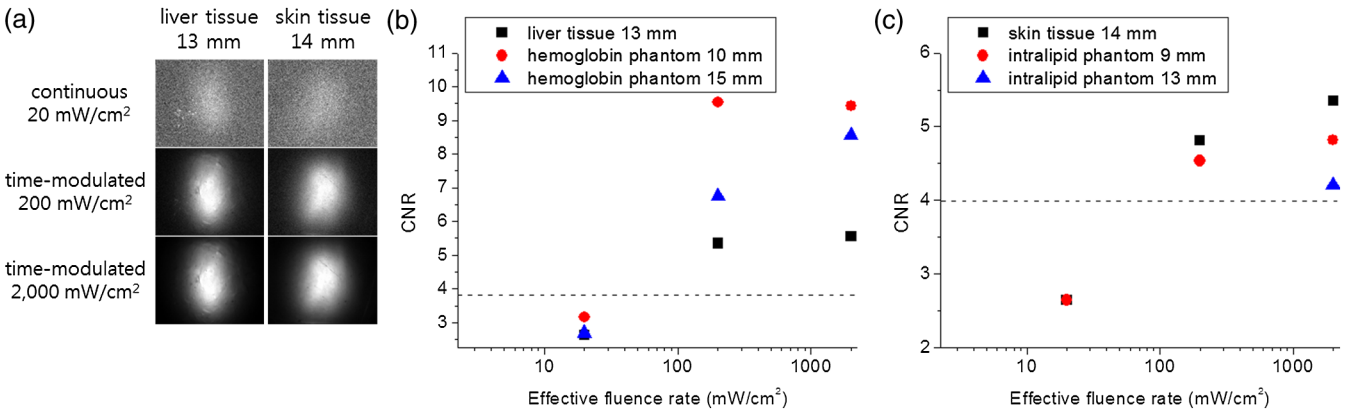

Fig. 3 (a) Near-infrared fluorescence images in biological tissue, (b) CNRs in 13 mm liver tissue and in hemoglobin phantoms (2 wt%), and (c) CNRs in 14 mm skin tissue and in intralipid phantoms (1 wt%). A 915 nm laser was used for continuous 20 mW/cm^2, time-modulated pulsed 200 and 2000 mW/cm^2 excitations. Horizontal axes in the plots are logarithmically scaled.

were technically undetectable [Figs. 3(b) and 3(c)]. Our previous liquid phantom experiments showed CNR values of 2.69 for the 15 mm hemoglobin phantom and 2.65 for the 9 mm intralipid phantom. It is noted that the liquid phantoms whose thicknesses were comparable to the liver and skin tissues also returned CNR values below the Rose criterion. As we increased the effective fluence rate to 10 or to 100 times higher, the QD cylinder under the liver or skin tissues was imaged vividly with the CNR values increased more than twofold [Fig. 3(a)]. The CNR values responded to the effective fluence rate change similarly to the real tissues and to the liquid phantoms, which confirms the validity of our liquid phantom model [Figs. 3(b) and 3(c)].

Our liquid and tissue phantom experiments demonstrate a significant increase in the QD imaging depth both in highly absorbing and highly scattering media by powering up the effective fluence rate using time-modulated pulsed excitation, which led us to further pursue small animal QD imaging experiments *in vivo*. A glass cylinder was filled with the PbS QD solution used for the liquid and tissue phantom experiments. Dimensions of the cylinder were 3 cm by 5 mm. It was inserted into the abdominal cavity of a female nude mouse parallel to the spinal column. Color and NIR fluorescence images were taken using an identical experimental condition as for the phantom experiments. In Fig. 4, the first column shows color images obtained from the color CCD, and the second to last columns display NIR images obtained by the InGaAs CCD. The top row in Fig. 4 shows the QD cylinder before the abdominal insertion. Continuous 20 mW/cm^2 excitation resulted in the cylinder image with a CNR of 11.0. Images by pulsed excitations were omitted because the conditions resulted in total saturations of the signal. The second to bottom rows in Fig. 4 show the images taken from ventral, dorsal, left, and right side directions. In the ventral view, images look similar regardless of the different excitations of a continuous 20 mW/cm^2, pulsed 200 and 2000 mW/cm^2. The ventral view direction requires only a shallow thickness from the outside, and as a result, the small effective fluence rate was sufficient for the imaging and no noticeable enhancement was observed by increasing the effective fluence rate. The case was quite contrary for the dorsal view. Continuous 20 mW/cm^2 excitation completely failed to image the QD cylinder. The pulse excitation of 200 mW/cm^2 began to visualize the QD cylinder with a CNR of 2.6, which is still below the criterion. It was only when the pulse excitation was increased to 2000 mW/cm^2 that the QD cylinder became visible with a CNR value over 4. The dorsal view needs very deep imaging depth through the bones and internal organs, which demands an increased effective fluence rate by pulsed excitations for the QD cylinder to be clearly imaged. Dorsal view images of the QD cylinder were dissected by a dark horizontal line, which is thought to be attributed to the vertebral column. The QD cylinder image was also severely distorted by the dispersions to both lateral sides, which is thought to originate from the different tissue thicknesses: deepest along the vertebral column line and becoming shallow from farther away laterally from the vertebral column. For the side views (left and right views), the QD cylinder is thought to require an intermediate imaging depth through some internal organs. The side views resulted in the most noticeable imaging capability enhancement by increasing the effective fluence rate. Under the continuous 20 mW/cm^2 excitation, the QD cylinder was hardly imaged with a CNR of 2.8. Upon the pulsed excitation of 200 or 2000 mW/cm^2, the CNR increased to a value between 7 and 8, which is more than two times the enhancement. However, the images were severely distorted by the internal organs and the contour of the body, which provided nonuniform depths. These QD *in vivo* imaging experiments demonstrate that the effective fluence rate increase using a time-modulated excitation system can effectively extend the imaging depth in a live animal system. The CNR could be enhanced over twofold, which is similar to the cases of liquid phantoms and tissues.

3.3 *Multiple Acquisition: Image Enhancement by Averaging*

A larger CNR value can be obtained for an image by increasing the camera integration time (or exposure time); however, excessively long integration time results in deterioration of the image quality and lowering of the CNR value, which originate from the overwhelming thermal noise. Image averaging of multiple acquisitions is a technique that can effectively increase the CNR value by avoiding the camera thermal noise issue. Averaging many images of an identical object has been widely used to enhance the image quality.[30] For example, the CNR of magnetic resonance imaging (MRI) image could be enhanced by averaging single trial MRI images, and the CNR of the averaged

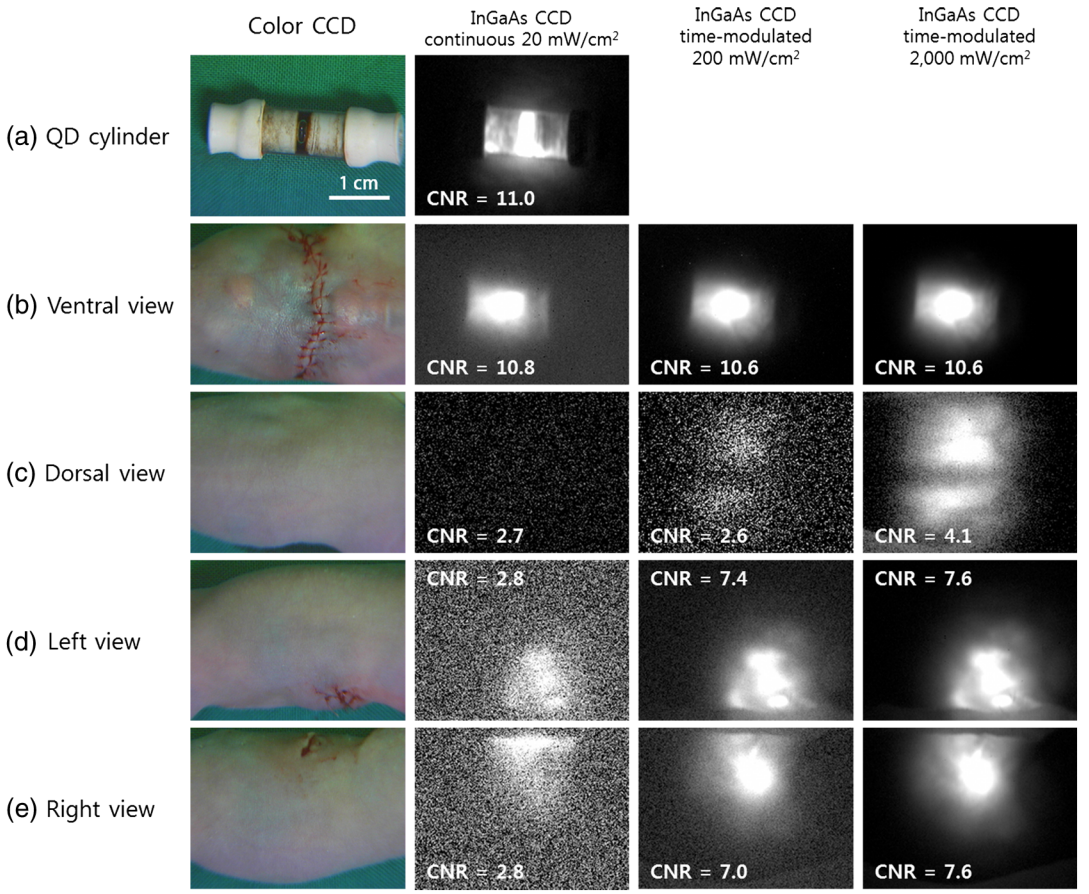

Fig. 4 Small animal (a nude mouse) whole-body imaging using near-infrared emitting QDs. (a) Image of a glass cylinder containing PbS QD solution. (b) Ventral view, (c) dorsal view, (d) left view, and (e) right view of the mouse were taken for imaging of the QD cylinder, which was inserted in the abdominal cavity. In all rows, first column: color charge-coupled device (CCD) images; second column: near-infrared InGaAs CCD images excited by 915 nm continuous laser at the fluence rate of 20 mW/cm^2; third column: InGaAs CCD images excited by 915 nm time-modulated laser at the effective fluence rate of 200 mW/cm^2; fourth column: InGaAs CCD images excited by 915 nm time-modulated laser at the effective fluence rate of 2000 mW/cm^2. Time-average intensities of the time-modulated light were 20 mW/cm^2, the same as that of the continuous excitation.

image was enhanced proportional to the square root of the number of averaged images when compared with that of a single trial image.[31,32] CNR enhancement can be achieved either by increasing the difference between the signal and background intensities or by decreasing the standard deviation of the background intensity. While increasing the integrating time of a camera can benefit both factors as described above, image averaging of multiple acquisitions is expected only related to the standard deviation of the background. As a result, the image enhancement by multiple acquisitions should be dependent on the characteristics of a single image, which, in turn, should be determined by the imaging conditions, such as the required imaging depth. To investigate the degree of image quality enhancement under different imaging conditions, particularly for our NIR SOW QD imaging, we have prepared a 1300 nm emitting QD cylinder sample under the 2 wt% hemoglobin or 1 wt% intralipid phantom. Over a thousand shots of the QD cylinder fluorescence images were taken as the phantom thickness was varied under identical experimental conditions, including the camera setting, exposure time of CCD, and excitation light intensity (continuous 915 nm laser excitation at 20 mW/cm^2). Each single image was taken using an optimal integrating time, which was <100 ms. Collecting 1000 image acquisitions took <2 min. The phantom thickness was varied from 0 to 13 mm for the hemoglobin and from 0 to 21 mm for the intralipid, respectively, and over 1000 images were taken and averaged with the multiple acquisitions of 1, 10, 100, or 1000 images for each thickness condition. The averaged images were obtained by averaging the multiple acquisitions pixel by pixel. The CNR values were compared for the averages from different numbers of acquisitions [Figs. 5(a) and 5(b)]. As expected, the CNR values decreased as the phantom thickness increased. At a given thickness condition, the CNR enhancement stood out only for the cases of intermediate thickness for both kinds of phantoms. CNR enhancement by increasing the average number of acquisitions was not observed for the cases of zero phantom thickness. The CNR enhancement increased with an increase in the phantom thickness until a certain point, and upon passing that thickness, the effect was reversed and the CNR enhancement became smaller until no enhancement was observed for very thick phantom cases. In our cases, the optimal intermediate phantom thickness was 9 mm for the hemoglobin phantom and 11 mm for the intralipid phantom. Figure 5(c) shows the QD cylinder fluorescence images for single shot and averaged images with the acquisitions

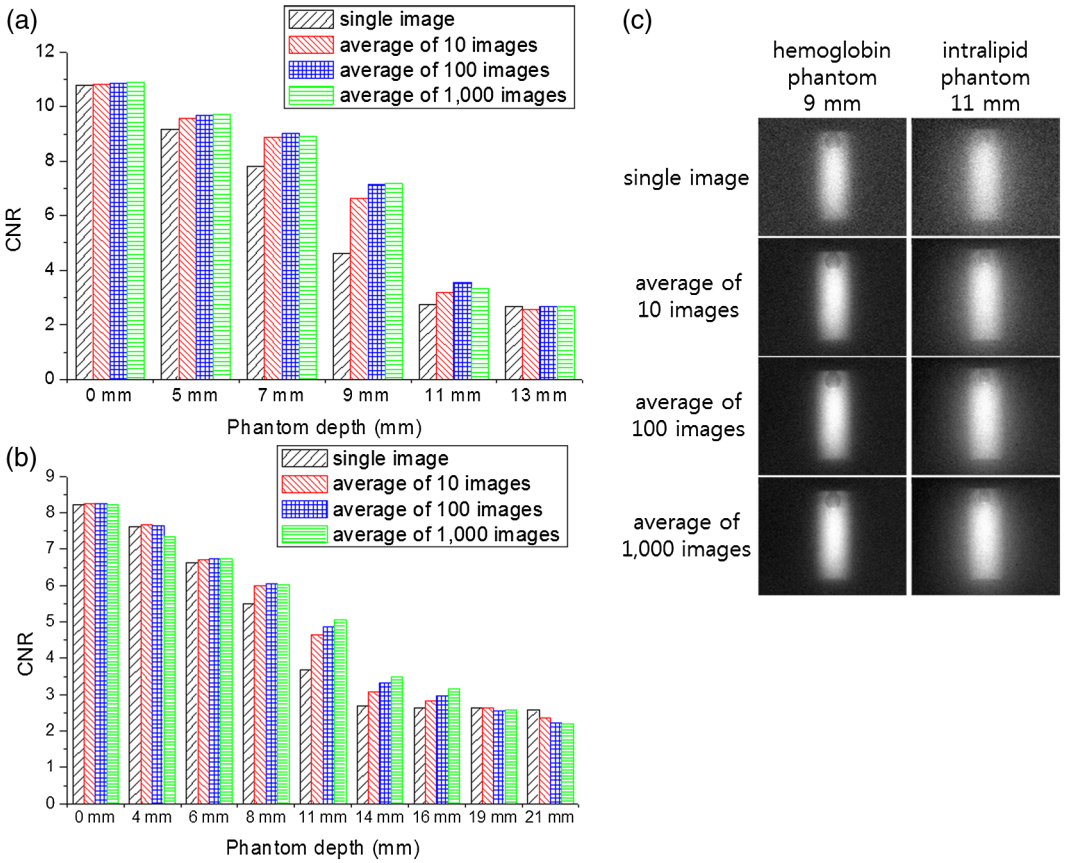

Fig. 5 Effects of image averaging in liquid phantoms. CNR of single or averaged images (a) in the 2 wt% hemoglobin phantom and (b) in the 1 wt% intralipid phantom. (c) Near-infrared fluorescence images of single or average or 10, 100, or 1000 acquisitions, in the 9 mm hemoglobin phantom or 11 mm intralipid phantom. A 915 nm continuous laser light was used to excite at the fluence rate of 20 mW/cm^2.

of 10, 100, and 1000 shots. For both phantom cases, the QD cylinder signal intensities did not change for different numbers of acquisitions, which means the brightness of the QD cylinder in the image did not change with the averaging process. It is noted that the background became more uniform and clearer on increasing the number of acquisitions. For the case of the 9 mm hemoglobin phantom, the CNR was 4.61 for the single shot and increased to 6.62, 7.13, and 7.18 when increasing the acquisitions to 10, 100, and 1000. For the case of the 11 mm intralipid, the CNR was 3.68, which is below the Rose criterion. The CNR increased to 4.64, 4.87, and 5.05 for the 10, 100, and 1000 acquisition averages. The CNR enhancement is thought to originate from the smaller standard deviation of the background intensity by averaging random thermal fluctuation noise. When the phantom depth is too shallow, there is not much room for improvement for the background, and as a result, the CNR enhancement is marginal. On the other hand, phantom cases that were too deep also showed marginal CNR enhancement because the signal intensity was too small, and thus, the small difference between the signal and background intensities dominated the CNR values. For both highly absorbing and highly scattering media, it was demonstrated that the CNR values could be enhanced nearly twofold by averaging multiple acquisitions. The high thermal noise level of the detector in NIR SOW is a major drawback when considering the SOW wavelength over the FOW. It is demonstrated that averaging multiple acquisitions can effectively alleviate this difficulty. For potential biomedical applications, multiple acquisitions should be accompanied by software-wise corrections that can eliminate the effect from motions over time, such as breathing.

4 Conclusion

QD imaging depth enhancement in NIR SOW was investigated by increasing the effective fluence rate using the criterion of CNR. The QD imaging depth under excitation of the continuous 20 mW/cm^2 laser was determined to be 10.3 mm for the 2 wt% hemoglobin phantom medium and 5.85 mm for the 1 wt% intralipid phantom. Time-modulated pulsed laser excitations allowed higher effective fluence rates while maintaining the same time-averaged fluence rate of 20 mW/cm^2, which is approved by the FDA for humans. The imaging depths of the SOW QDs were extended upon increasing the effective fluence rate. For both phantoms, the imaging depths were enhanced by more than two times under a 100 times higher effective fluence rate than the cases of a continuous 20 mW/cm^2. The QD imaging capabilities in SOW were also studied using biological tissues such as bovine liver and porcine skin to validate our liquid phantoms. The QD imaging CNR values increased by more than two times upon increasing the effective fluence rate from 20 to 2000 mW/cm^2, which accords with our liquid phantom results. QD NIR SOW imaging was further tested using a small animal *in vivo*. A QD sample was inserted into the abdomen of a mouse, and the tissue depths to the QD sample were varied by changing

the imaging direction to ventral, dorsal, or to the side directions. The imaging depth enhancement by increasing the effective fluence rate using pulsed excitations could be successfully applied to the *in vivo* system. For an example, the dorsal direction imaging, which required the largest imaging depth through the vertebral column and many internal organs, showed the completely undetectable QD signal under continuous 20 mW/cm^2 excitation, but was dramatically enhanced by increasing the effective fluence rate by 100 times and became detectable with the enhanced CNR value exceeding the Rose criterion. As another strategy of enhancing the QD imaging in NIR SOW other than the effective fluence rate control by excitation time-modulation and synchronization with the detector, multiple image acquisitions and averaging were investigated. The high thermal noise level is a major hurdle in NIR SOW QD imaging. We have demonstrated that the detector noise problem can be circumvented by the image averaging. Under an optimal condition, the CNRs could be enhanced nearly twofold by averaging multiple acquisitions. We are hopeful that using more than one of the strategies, such as higher effective fluence rate and averaging multiple acquisitions, can greatly boost the QD imaging capability in NIR SOW. This advance can lead us to deep tissue penetration and multiplexed QD imaging in SOW for numerous applications in biological studies, such as real-time *in vivo* longitudinal animal investigations for tumor growth and metastasis. With the advent of more biocompatible NIR SOW QDs, such as Ag_2S QD, medical applications such as sensitive diagnoses and intraoperative guidance are also promising for NIR SOW QDs.

Acknowledgments

This research was supported by a grant of the Korea Health Technology R&D Project through the Korea Health Industry Development Institute (KHIDI), funded by the Ministry of Health & Welfare (HI12C1642) and by a grant from the National R&D Program for Cancer Control, Ministry for Health and Welfare (1320220), Republic of Korea.

References

1. M. Roy et al., "Effect of tissue optics on wavelength optimization for quantum dot-based surface and subsurface fluorescence imaging," *J. Biomed. Opt.* **17**(2), 026002 (2012).
2. P. Lenz, "Fluorescence measurement in thick tissue layers by linear or nonlinear long-wavelength excitation," *Appl. Opt.* **38**(16), 3662–3669 (1999).
3. J. V. Frangioni, "In vivo near-infrared fluorescence imaging," *Curr. Opin. Chem. Biol.* **7**(5), 626–634 (2003).
4. R. Weissleder, "A clearer vision for in vivo imaging," *Nat. Biotechnol.* **19**(4), 316–317 (2001).
5. A. M. Smith, M. C. Mancini, and S. Nie, "Bioimaging: second window for in vivo imaging," *Nat. Nanotechnol.* **4**(11), 710–711 (2009).
6. N. Won et al., "Imaging depths of near-infrared quantum dots in first and second optical windows," *Mol. Imaging* **2011**(5), 1–2 (2011).
7. Y. T. Lim et al., "Selection of quantum dot wavelengths for biomedical assays and imaging," *Mol. Imaging* **2**(1), 50–64 (2003).
8. J. O. Escobedo et al., "NIR dyes for bioimaging applications," *Curr. Opin. Chem. Biol.* **14**(1), 64–70 (2010).
9. D. J. Naczynski et al., "Rare-earth-doped biological composites as in vivo shortwave infrared reporters," *Nat. Commun.* **4**, 1–10 (2013).
10. K. Welsher, S. P. Sherlock, and H. Dai, "Deep-tissue anatomical imaging of mice using carbon nanotube fluorophores in the second near-infrared window," *Proc. Natl. Acad. Sci.* **108**(22), 8943–8948 (2011).
11. I. Moreels et al., "Size-tunable, bright, and stable PbS quantum dots: a surface chemistry study," *ACS Nano* **5**(3), 2004–2012 (2011).
12. T. Pons et al., "Cadmium-free $CuInS_2$/ZnS quantum dots for sentinel lymph node imaging with reduced toxicity," *ACS Nano* **4**(5), 2531–2538 (2010).
13. L. Li et al., "Highly luminescent CuInS2/ZnS core/shell nanocrystals: cadmium-free quantum dots for in vivo imaging," *Chem. Mater.* **21**(12), 2422–2429 (2009).
14. K. T. Yong et al., "Imaging pancreatic cancer using bioconjugated InP quantum dots," *ACS Nano* **3**(3), 502–510 (2009).
15. J. Bang et al., "ZnTe/ZnSe (core/shell) type-II quantum dots: their optical and photovoltaic properties," *Chem. Mater.* **22**(1), 233–240 (2010).
16. T. Torimoto et al., "Facile synthesis of ZnS-$AgInS_2$ solid solution nanoparticles for a color-adjustable luminophore," *J. Am. Chem. Soc.* **129**(41), 12388–12389 (2007).
17. Y. Zhang et al., "Ag_2S quantum dot: a bright and biocompatible fluorescent nanoprobe in the second near-infrared window," *ACS Nano* **6**(5), 3695–3702 (2012).
18. Y. P. Du et al., "Near-infrared photoluminescent Ag_2S quantum dots from a single source precursor," *J. Am. Chem. Soc.* **132**(5), 1470–1471 (2010).
19. A. K. Dunn et al., "Influence of optical properties on two-photon fluorescence imaging in turbid samples," *Appl. Opt.* **39**(7), 1194–1201 (2000).
20. R. Steiner, "Laser-tissue interactions," in *Laser and IPL Technology in Dermatology and Aesthetic Medicine*, C. Raulin and S. Karsai, Eds., pp. 23–36, Springer, Berlin Heidelberg (2011).
21. Food and Drug Administration, "Performance standards for light-emitting products," http://www.fda.gov (9 January 2014).
22. M. A. Hines and G. D. Scholes, "Colloidal PbS nanocrystals with size-tunable near-infrared emission: observation of post-synthesis self-narrowing of the particle size distribution," *Adv. Mater.* **15**(21), 1844–1849 (2003).
23. R. C. Gonzalez, R. E. Woods, and S. L. Eddins, *Digital Image Processing Using MATLAB*, Pearson Education India (2004).
24. A. Rose, *Vision: Human and Electronic (Optical Physics and Engineering)*, Springer, New York (1973).
25. X. Song et al., "Automated region detection based on the contrast-to-noise ratio in near-infrared tomography," *Appl. Opt.* **43**(5), 1053–1062 (2004).
26. D. R. Larson et al., "Water-soluble quantum dots for multiphoton fluorescence imaging in vivo," *Science* **300**(5624), 1434–1436 (2003).
27. B. K. Andrasfalvy et al., "Quantum dot-based multiphoton fluorescent pipettes for targeted neuronal electrophysiology," *Nat. Methods* **11**(12), 1237–1241 (2014).
28. O. E. Semonin et al., "Absolute photoluminescence quantum yields of IR-26 dye, PbS, and PbSe quantum dots," *J. Phys. Chem. Lett.* **1**(16), 2445–2450 (2010).
29. W. F. Cheong, S. A. Prahl, and A. J. Welch, "A review of the optical properties of biological tissues," *IEEE J. Quantum Electron.* **26**(12), 2166–2185 (1990).
30. J. C. Russ, *The Image Processing Handbook*, 6th ed., CRC Press, Boca Raton (2011).
31. H. L. Liu et al., "The effects of single-trial averaging on the temporal resolution of functional MRI," *Magn. Reson. Imaging* **24**(5), 597–602 (2006).
32. J. Sijbers et al., "Quantification and improvement of the signal-to-noise ratio in a magnetic resonance image acquisition procedure," *Magn. Reson. Imaging* **14**(10), 1157–1163 (1996).

Yebin Jung is a PhD candidate at the Department of Chemistry, Pohang University of Science and Technology, where she received her MSc degree in chemistry in 2012. Her major interest is near-infrared fluorescence imaging using quantum dot–based probes.

Sungjee Kim is a PhD in physical chemistry and has a broad interest across chemistry, biology, and medicine. He is focused on studying light-nanoparticle interactions as aiming potential applications toward practical medical arena.

Biographies for the other authors are not available.